IEEE Access
Multidisciplinary | Rapid Review | Open Access Journal

Received November 3, 2020, accepted November 19, 2020, date of publication November 23, 2020,
date of current version December 7, 2020.

Digital Object Identifier 10.1109/ACCESS.2020.3039927

Reconstruction of X-Ray Fluorescence Computed Tomography From Sparse-View Projections via L1-Norm Regularized EM Algorithm

JUNWEI SHI, DAIKI HARA, WENSI TAO, NESRIN DOGAN, ALAN POLLACK, AND JOHN CHETLEY FORD
Department of Radiation Oncology, Miller School of Medicine, University of Miami, Miami, FL 33136, USA
Corresponding author: Junwei Shi (jxs1725@med.miami.edu)

This work was supported by the Sylvester Cancer Center and Department of Radiation Oncology in University of Miami.

ABSTRACT X-ray fluorescence computed tomography (XFCT) as a molecular imaging modality can simultaneously identify the localization and quantify the concentration of high-atomic-number contrast agents such as gold nanoparticles (GNPs). Commonly used benchtop pencil-beam XFCT, consisting of a polychromatic x-ray source and a single-pixel spectrometer, suffers from long scanning time and high imaging dose. Sparse-view strategy benefits XFCT to reduce both scanning time and imaging dose. Nevertheless, its reconstruction undergoes ill-posedness induced by the compressive sampling. To preserve consistent imaging quality for sparse-view XFCT, we proposed an iterative Bayesian algorithm based on L1-norm constraint, wherein the L1-norm regularization is included in the one-step-late expectation maximization (OSL-EM) algorithm with regularization parameter determined based on L-curve criteria. The proposed algorithm was verified by imaging a 3-cm-diameter water phantom with 4 inserts containing GNP solutions with concentrations of 0.02, 0.04, 0.08, and 0.16 wt.%, on an in-house-developed dual-modality transmission CT and XFCT system. Different numbers (i.e. 36, 18, 9, and 6) of projection views were used for XFCT reconstruction, to evaluate the performance of various reconstruction algorithms. L1-regularized EM algorithm demonstrated the consistent robustness to suppress background artifacts and localize low-concentration GNPs (0.02 wt.%) with submillimeter accuracy, when the number of projection views reduces from 36 to 9. Moreover, our method's potential for small tumor spare-view XFCT imaging was validated on a mouse surgically implanted with a 6-mm GNP target.

INDEX TERMS X-ray fluorescence computed tomography, image reconstruction, sparse projection view, gold nanoparticles.

I. INTRODUCTION

X-ray fluorescence computed tomography (XFCT) as a promising molecular imaging modality has attracted broad interests, with the recent emergence of various biomedical applications of high-Z metal (e.g. Gadolinium and Gold) nanoparticles (NPs) [1], [2]. These NPs have been intensively investigated in nanomedicine as imaging agents, biosensor, drug carrier and therapeutic agents [3]. By detecting the element-specific x-ray fluorescence (XRF) photons, XFCT can sensitively identify and quantify the distribution of high-Z NPs *in vivo*, which is indispensable in drug development and oncology studies.

The associate editor coordinating the review of this manuscript and approving it for publication was Mohamad Forouzanfar.

Early-stage XFCT was typically performed using synchrotron, to take advantage of the high brilliance and collimation of monochromatic x-rays for high sensitivity analysis in material and biomedical sciences [4]–[7]. More recently, benchtop systems implemented with polychromatic diagnostic x-ray sources have been proposed to improve the accessibility of *in vivo* XFCT imaging [8]–[14]. However, the low photon flux of the polychromatic source leads to the low efficiency of XRF photon emission with long detector acquisition time. Meanwhile, for the vast majority of XFCT systems equipped with one single-pixel detector, the long scanning time is inevitable because the tomographic data are acquired from sequential translation and rotation scanning of objects. The cost of significantly long scanning time is the decreased XFCT imaging throughput, which will be a

major bottle neck when large scale preclinical studies are needed.

There have been ongoing research efforts by many research groups to develop various benchtop XFCT systems with short imaging time. By simulating on a Monte Carlo (MC) model with a polychromatic cone-beam source and collimated detector arrays, Jones and Cho theoretically validated the feasibility of reduction (ten-fold) in scanning time [15]. Jiang *et al* simulated the similar strategy on XFCT implemented with polychromatic sheet beam and linear collimated detector arrays [16]. Dunning and Bazalova-Carter proposed a pencil-beam XFCT setup with 8 carefully arranged spectrometers for parallel XRF collection and validated its feasibility through MC simulation [17]. Li *et al* developed a full-field fan-beam XFCT system with a conventional x-ray tube and a pinhole collimated linear detector array for fast NP imaging [18]. This system was successfully used for quantitative imaging of Gadolinium NPs in mice with 7.5 min imaging time per slice [2]. By using polychromatic fan beam and a pinhole collimated 2D cadmium zinc telluride (CZT) camera, Jung *et al* realized dynamic *in vivo* XRF imaging of Gold nanoparticles (GNPs) in living mice with 2 min imaging time per slice [19]. However, the pinhole collimator used in the aforementioned XFCT systems inevitably constrains the XRF photons acquired by the detectors, which further limits the XFCT imaging sensitivity. To enhance the XRF photon acquisition, multi-pinhole strategy used in SPECT can be adopted to improve the signal-to-noise ratio of XFCT imaging [20]. Moreover, Vernekohl *et al* proposed using Compton cameras to recover NP spatial information without the loss of sensitivity associated with detector collimation [21]. Based on their MC simulation on a human-size Medical Internal Radiation Dose (MIRD) phantom, the XFCT imaging time could be reduced by a factor of 45 with the use of a Compton camera. Besides, to speed up benchtop XFCT imaging, specific x-ray sources (e.g. polycapillary x-ray source [22], and liquid-metal-jet x-ray source [23]) with high photon fluence rate was employed by different research groups.

The strategies mentioned above achieve XFTC imaging acceleration by implementing hardware upgrades (including x-ray source and XRF detector), which will inevitably enhance the system cost. La Rivière *et al* proposed a reduced-scan scheme for the conventional pencil-beam XFCT with one single-pixel detector, by utilizing the data redundancy in the 360^{o} attenuated Radon Transform [24]. In this scheme, only the half of the object closest to the XRF detector is scanned at each projection view, which can speed up the XFCT scanning by twice. Moreover, analogous to the sparse-view and limited-angle CT imaging [25], an intuitive and effective strategy for fast XFCT imaging is reducing the number of projections. In the sparse-view scenario, the tomographic image is recovered from the sparse projection views evenly sampled in the 360-degree (i.e. full rotation) span. In the limited-angle scenario, tomographic imaging is realized through the projections only distributing in a limited-angle (<360 degree) span. In the both strategies, only a limited number of tomographic XRF projections are used for internal high-Z NP imaging. Meanwhile, sparse-view or limited-angle strategy can reduce the XFCT imaging dose, hence enabling long-term *in vivo* functional imaging with weak radiation interference from XFCT itself. However, sparse-view or limited-angle XFCT reconstruction suffers from the aggravated ill-posedness.

In this study, to maintain the robust imaging performance for sparse-view XFCT, sparsity prior in the form of L1-norm regularization was incorporated as a penalty function to enhance the robustness against artifacts. For XFCT tumor imaging, the reconstructed image tends to be sparse since the metal NPs are always designed to selectively accumulate in tumors by means of active targeting techniques [26]. The L1 regularization-based XFCT reconstruction problem was expressed as a Bayesian objective function and solved using the Green's one-step-late EM algorithm because it is user-friendly and easy to implement. Also, an L-curve method was implemented to automatically select the optimal regularization parameter for the proposed L1-EM algorithm. The performance of the proposed algorithm was evaluated by imaging a water phantom with 4 inserts containing Gold nanoparticles (GNPs) with different concentrations. Then the proposed L1-EM algorithm was applied for XFCT reconstruction using different numbers of projections. Results show that compared with the traditional ML-EM algorithm, the proposed algorithm outperforms in robustness against background artifacts when the number of projection views reduced from 36 to 9, which significantly reduces the scanning time and imaging dose of the benchtop XFCT.

II. MATERIALS AND METHODS

A. BENCHTOP XFCT EXPERIMENT SETUP

Figure 1A shows the benchtop dual-modality system, which allows pencil-beam XFCT and cone beam computed tomography (CBCT) imaging. The XFCT subsystem consists of an x-ray tube (XRS-225, COMET, Flamatt, Switzerland), a pencil-beam collimator, an Aluminum (Al) filter, a rotation stage (CR1-Z7, ThorLabs, Newton, NJ, USA), a translation stage (MTS50-Z8, ThorLabs, Newton, NJ, USA), and an XRF detector (Fast SDD, Amptek, Bedford, USA). The pencil-beam collimator was 3D printed using stainless steel and can generate a 2-mm beam at the imaging isocenter. A 2-mm-thick Al filter was used to suppressed tungsten L_{β} XRF (9.67keV) from the x-ray source, preventing the interference on the gold L_{α} XRF (9.71keV). The motorized rotation and translations stages were used to move objects along the pencil beam for tomographic scanning. The single-pixel XRF detector was placed at 120 deg with respect to the excitation beam to reduce the Compton background. CBCT shares the x-ray tube and rotation stage with XFCT. A flat panel detector (PerkinElmer, Waltham, MA, USA) with 20×20 cm^2 area and 200 μm pitch was employed to collect transmission x-ray projections for CBCT imaging.

A small-animal-sized water phantom of 4.5 cm height and 3 cm diameter was customized for XFCT imaging

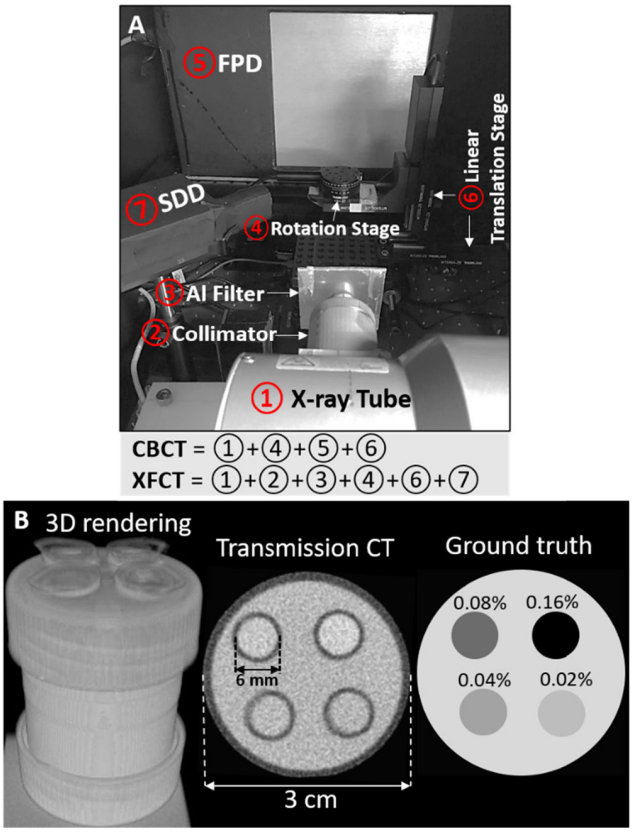

FIGURE 1. (A) Dual-modality benchtop XFCT and CBCT imaging system. SDD: Silicon Draft Detector. FPD: Flat Panel Detector. (B) The water phantom with 4 inserts containing GNPs of different concentrations: (Left) 3D rendering of phantom CT, (Middle) axial CT slice, and (Right) true distribution of 4 GNP targets in the phantom.

in this study (Fig. 1B). The phantom was inserted with 4 tubes (6 mm diameter) containing GNP solutions with different concentrations (0.16 wt.%, 0.08 wt.%, 0.04 wt.%, and 0.02 wt.%). The commercially available 15-nm-diameter GNPs (AuroVist, Nanoprobes, Yaphank, NY, USA) were used and diluted with deionized water. Under the current configuration, the XFCT collects projection data in the same way as the first-generation CT. The collimated incident beam was produced by the x-ray tube operated at 1-mm-focal-spot setting with 64 kVp and 10 mA. The translation step size for the phantom was 1.5 mm, and the acquisition time per XRF projection was set to 30 sec. To fully cover the width of phantom, 21 translation steps were performed. The rotation stage was rotated by 10^o for the full 360^o coverage, to ensure that enough projection data are collected for the normal XFCT imaging. Thus, there were 36×21 measured projections in total. Then the projections for sparse-view XFCT imaging could be acquired by compressively sampling the 36-angle data. For example, an 18-view dataset (size: 18×21) can be acquired by sampling the measured 36-view dataset every two angles, and so on.

In this study, we evaluated the XFCT imaging quality with 36, 18, 9, and 6 projection views, respectively. Transmission CBCT provides a benchmark to evaluate the localization accuracy for the sparse-view XFCT. Regarding CBCT imaging, the x-ray tube was operated at 1-mm-focal-spot setting with 45 kVp and 2.5 mA. And a 0.5-mm-thick Cu filter was used to adjust the incident beam spectrum. The transmission x-ray projections were acquired by the FPD with 124 ms exposure time at every 1^o step over a 360^o rotation. Given the current CBCT system with a circular x-ray source trajectory, the 3D CBCT images were directly reconstructed from 2D projections using the Feldkamp-Davis-Kress (FDK) algorithm which is a 3D extension of the 2D fan-beam filtered backprojection (FBP) method mainly consisting of filter convolution and backprojection [27].

B. L1-EM ALGORITHM

Based on a set of measured sinograms (or arranged projection data), the XFCT reconstruction problem is formulated as:

$$P_i = \sum_j W_{i,j} X_j \tag{1}$$

where $W_{i,j}$ is the system matrix representing the probability that an XRF photon will be emitted from pixel X_j and detected in the projection element P_i, under the ith pencil beam excitation. Given the primary and fluorescence photon attenuation, the system matrix element is calculated as [28]:

$$W_{i,j} = d_{i,j} e^{-\mu_{ex} l_{ex}} e^{-\mu_f l_f} \tag{2}$$

where $d_{i,j}$ is the intersection length of the pencil beam i with pixel j. μ_{ex} and μ_f are the x-ray photon attenuation coefficients in water for the primary beam and XRF, respectively. l_{ex} denotes the distance that pencil beam i travels through the objects before reaching pixel j, and l_f is the distance through the phantom XRF photons travel from pixel j to the detector.

XFCT reconstruction is an inverse problem to recover the tomographic distribution of NPs (i.e. X) throughout the object from the collected sinogram (i.e. P). This goal can be equivalent to maximizing the posterior probability distribution according to the Bayesian paradigm [29]. The objective function is summarized by:

$$Prob(X|P) = \frac{Prob(P|X)Prob(X)}{Prob(P)} \tag{3}$$

Taking the logarithm yields:

$$ln\,(Prob\,(X|P)) = ln\,(Prob\,(P|X)) + ln\,(Prob\,(X)) - ln\,(Prob\,(P)) \tag{4}$$

where the first term on the right-hand side of equation is the likelihood function, and the second term denotes the prior constraints about the image X. As the third term in (4) has nothing to do with the unknowns X, it can be eliminated.

For XFCT imaging, the number of XRF photons emitted from each pixel obeys the Poisson probability distribution. We define $c_{i,j}$ as a Poisson random variable to represent the count of XRF photons emitted from pixel j under the

excitation of pencil beam i. Then the likelihood function is:

$$Prob(P|X) = \prod_{i,j} e^{-W_{i,j}X_j} \frac{(W_{i,j}X_j)^{c_{i,j}}}{c_{i,j}!} \tag{5}$$

In order to improve the reconstruction robustness against artifacts, we adopted L1 norm as the prior constraint for the sparse-view XFCT inverse problem. Thus, the Bayesian objective function is crystallized as:

$$\begin{aligned}\mathbf{L}(X) &= \ln(\prod_{i,j} e^{-W_{i,j}X_j} \frac{(W_{i,j}X_j)^{c_{i,j}}}{c_{i,j}!}) + \lambda \|X\|_1^1 \\ &= \sum_{i,j} (c_{i,j} \ln(W_{i,j}X_j) - W_{i,j}X_j) - \sum_{i,j} \ln(c_{i,j}!) + \lambda \|X\|_1^1\end{aligned} \tag{6}$$

The second summation term in (6) does not contain the X to be estimated, therefore it can be removed without changing the maximum-likelihood problem. Then the Bayesian objective function becomes:

$$\mathbf{L}(X) = \sum_{i,j} (c_{i,j} \ln(W_{i,j}X_j) - W_{i,j}X_j) + \lambda \|X\|_1^1 \tag{7}$$

To eliminate the random variable $c_{i,j}$ in (7), $c_{i,j}$ is replaced by its expected value ($E(c_{i,j})$) using projection data P_i and current image estimate X_j:

$$E(c_{i,j}|P_i, X^{current}) = \frac{W_{i,j}X_j^{current}}{\sum_k W_{i,k}X_k^{current}} P_i \tag{8}$$

Then the XFCT reconstruction inverse problem is to maximize the following objective function:

$$\mathbf{L}(X) = \sum_{i,j} (\frac{W_{i,j}X_j^{current}}{\sum_k W_{i,k}X_k^{current}} P_i \ln(W_{i,j}X_j) - W_{i,j}X_j) + \lambda \|X\|_1^1 \tag{9}$$

By taking the derivative of (9) with respect to X_j and setting the derivatives to zero, the XFCT image can be reconstructed using the iterative Green's one-step-late algorithm:

$$X_j^{next} = \frac{X_j^{current}}{\sum_i W_{i,j} + \lambda \frac{\partial(\|X^{current}\|_1^1)}{\partial X_j^{current}}} \sum_i W_{i,j} \frac{P_i}{\sum_k W_{i,k}X_k^{current}} \tag{10}$$

where λ is the regularization parameter controlling the trade-off between data fidelity $\|\text{WX-P}\|_2^2$ and penalty constraint $\|X\|_1^1$. When $\lambda = 0$, the L1-EM algorithm (i.e. (10)) is reduced to the translational ML-EM algorithm:

$$X_j^{next} = \frac{X_j^{current}}{\sum_i W_{i,j}} \sum_i W_{i,j} \frac{P_i}{\sum_k W_{i,k}X_k^{current}} \tag{11}$$

The L1 norm is calculated globally, hence it possesses the advantage of global reduction of background artifacts. Nevertheless, this merit depends on the choice of an appropriate regularization parameter. Different λ values affect the XFCT reconstruction quality. This can be representatively seen from Fig. 2 displaying the XFCT results for the water phantom reconstructed from 36-view projections using the L1-EM algorithm with various λ values. If λ is small (Fig. 2(a) and 2(b)), there exists serious artifacts in the center region of the phantom. As shown in the histograms (Fig. 2 lower row), these artifacts were gradually eliminated with the increasing of λ value. However, the reconstructed image is overly sparsified, thus losing useful information on the reconstrued targets (Fig. 2(d)).

In this study, an L-curve criterion is adopted to automatically select optimal λ. For the L1-EM algorithm, L-curve is a plot between the L1 norm of the regularized solution ($\|X\|_1^1$) versus the Euclidean norm of the corresponding residual ($\|\text{WX-P}\|_2^2$) for a range of values of λ. As an example, Fig. 3(a) shows the L-curve for the reconstruction of the water phantom from 36-angle projections using L1-EM algorithm with various λ values. The maximum curvature of the L-curve is used to objectively characterize the corner of the L-curve [30]. As shown in the curvature plot (Fig. 3B), the L-curve curvature reaches its maximum when $\lambda = 0.25$. As displayed in Fig. 2(c), the reconstructed image corresponding to $\lambda = 0.25$ exhibits good balance between reducing background artifacts and holding image fidelity, indicating the reliability of the L-curve criterion. For comparison, both the conventional ML-EM (11) and the proposed L1-EM (10) algorithms were used to reconstruct an axial XFCT image consisting of 3600 pixels (0.5 mm × 0.5 mm pixel size).

C. IMAGE ANALYSIS

The reconstructed XFCT images were normalized to the mean XRF signal from a vial containing 0.16 wt.% GNPs. Then background noise in the reconstructed image, defined as the standard deviation of the pixel values in a 6-mm-diameter circle in the center of phantom, was employed to assess the reconstruction quality [31]. Additionally, CBCT was adopted as a benchmark to evaluate the localization accuracy of XFCT reconstruction, wherein the localization error was calculated as the Euclidean distance between the centroids of the XFCT target and the CBCT target. As shown in Fig. 1B, the CBCT image demonstrates the clear contour of the small tube with GNP solution. Therefore, the target centroids can be directly identified from the CBCT image as the benchmark. To calculate the XFC target centroids, the XFCT image was equally divided into four quarters, and then the four targets were segmented based on a 30threshold of the maximum in each quarter.

III. RESULTS

Different numbers of projection views were used for XFCT reconstruction to evaluate the accuracy and robustness of the proposed algorithm. The sinograms corresponding to 36, 18, 9, and 6 projection views are presented in Fig. 4 top row, respectively. Accordingly, the size of dataset used for XFCT reconstruction reduced from 36 × 21 to 18 × 21, 9 × 21, and

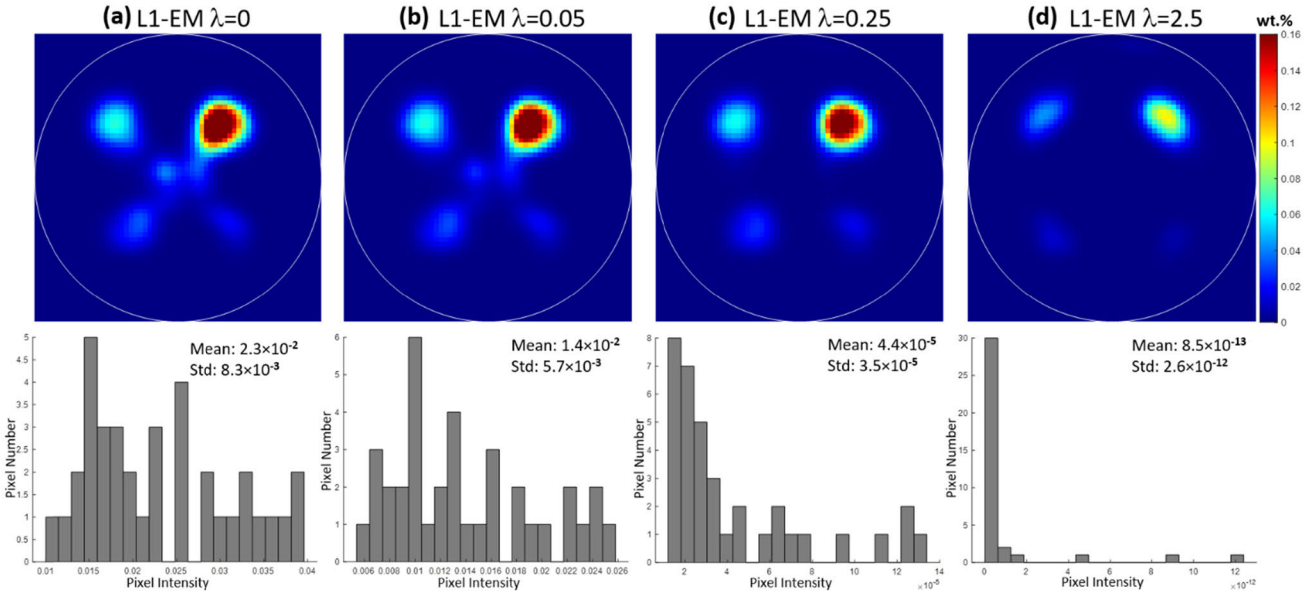

FIGURE 2. (Upper row) Reconstruction results for 4-target water phantom from 36-view projections using L1-EM with different regularization parameter λ. (Lower row) Histogram of background artifacts in the region defined as a 6-mm-diameter circle in the center of phantom.

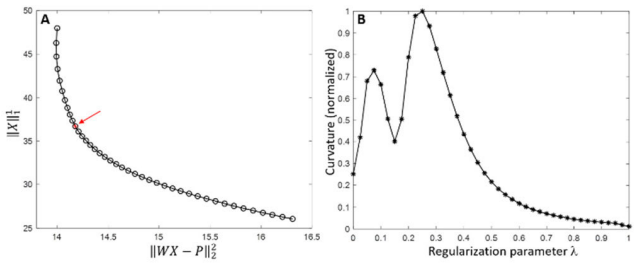

FIGURE 3. (A) L-curve for the reconstruction of the water phantom from 36-view projections using L1-EM algorithm with various regularization parameters. From top left to down right, the circles correspond to difference λ values from 0 to 1 with 0.025 interval. The red arrow indicates the optimal point on the L-curve, corresponding to $\lambda = 0.25$. (B) Plot of L-curve curvature versus λ values, where the peak appears at $\lambda = 0.25$.

6×21, which gradually increases the ill-posedness of the XFCT reconstruction inverse problem. Based on the L-curve criterion, the L1-EM regularization parameters in (10) were determined as $\lambda = 0.25$, 0.15, 0.10, and 0.05, respectively, for the XFCT reconstruction using 36, 18, 9, and 6 projection views. The reconstructed XFCT images from different numbers of projection views are presented in Fig. 4 middle and bottom rows. Although ML-EM can recover the four GNP targets, there exists obvious artifacts in the center region of the phantom, which will inevitably induce false positive detection. These artifacts are induced by the measure noise in sinograms, as well as by the ill-posedness of the XFCT reconstruction inverse problem. By contrast, the L1-EM algorithm reconstructed images with consistently reduced artifacts, even using only 6 projection angles.

The background noise values corresponding to the images reconstructed by ML-EM and L1-EM are presented in Fig. 5A. According to the results, the background noise in the images reconstructed by L1-EM is up to two order of magnitude smaller than that corresponding to ML-EM. As shown in Fig. 4, the background artifacts in the 9-view ML-EM reconstruction exhibits higher pixel intensity and more concentrated distribution, compared to other spare-view ML-EM reconstruction. That results in the highest ML-EM background noise (in Fig. 5A), which was quantified as the standard deviation in a region of interest herein, for the 9-projection-view XFCT.

Figure 5B shows the localization errors of the four GNP targets reconstructed from different number of projections using both ML-EM and L1-EM algorithms. As shown, L1-EM algorithm accurately localized the four GNP targets with <0.6 mm deviation when the number of projection views decreased from 36 to 9. For the 6-view L1-EM reconstruction, GNP targets with concentration of 0.04∼0.16 wt.% were localized with submillimeter precision, while the 0.02 wt.% target was recovered with >1mm localization error. Compared to L1-EM, ML-EM demonstrated much larger localization error especially for the low-concentration targets (i.e. 0.04 wt.% and 0.02 wt.%). Moreover, as shown in Fig. 4, the background artifacts in 9-view ML-EM reconstruction concentrate to a small region, reducing its influence on the low-concentration target localization. That also helps explain why the 0.02 wt.% target demonstrates the smallest localization error in 9-view XFCT, among all the ML-EM sparse-view XFCT reconstructions (Fig. 5B).

To investigate our method's potential for small tumor observability, a small sphere was surgically implanted into a euthanized mouse (Fig 6). A small hollow sphere (diameter: 6 mm) was 3D printed on the Ultimaker

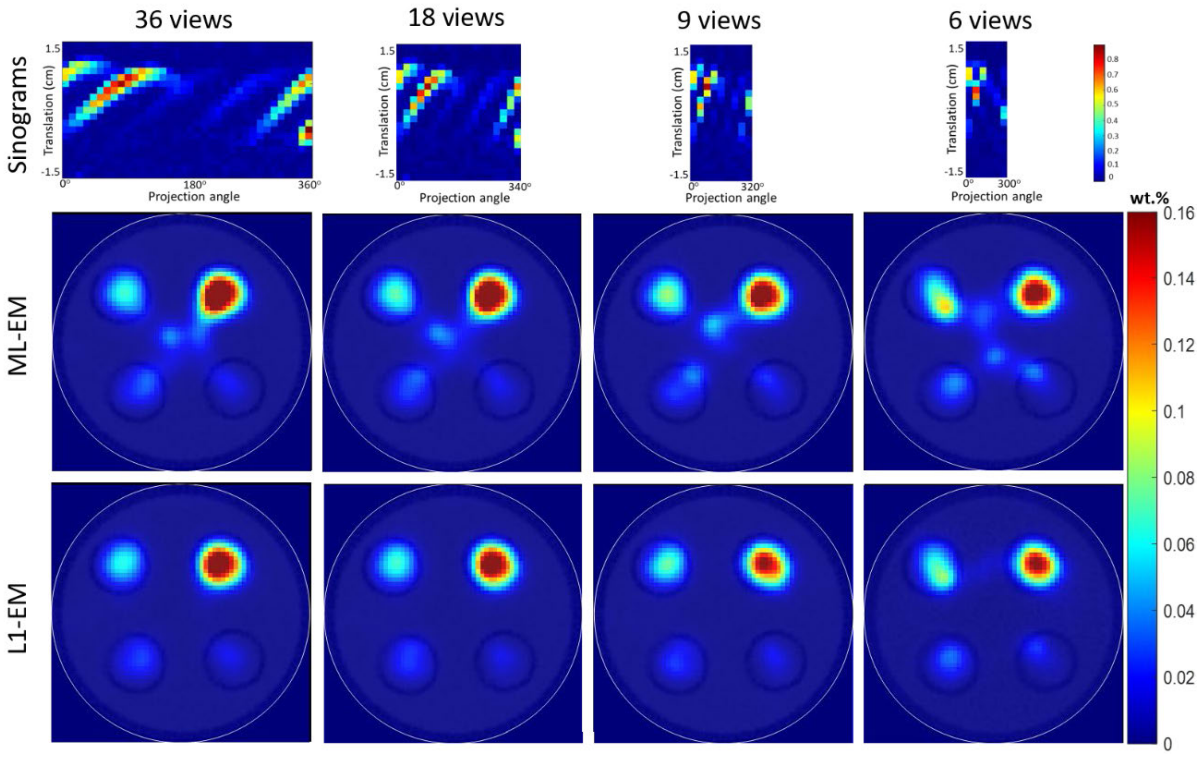

FIGURE 4. XFCT images reconstructed by different EM algorithms, in the scenarios with different number of projection views. The reconstructed XFCT images were fused with CBCT slice.

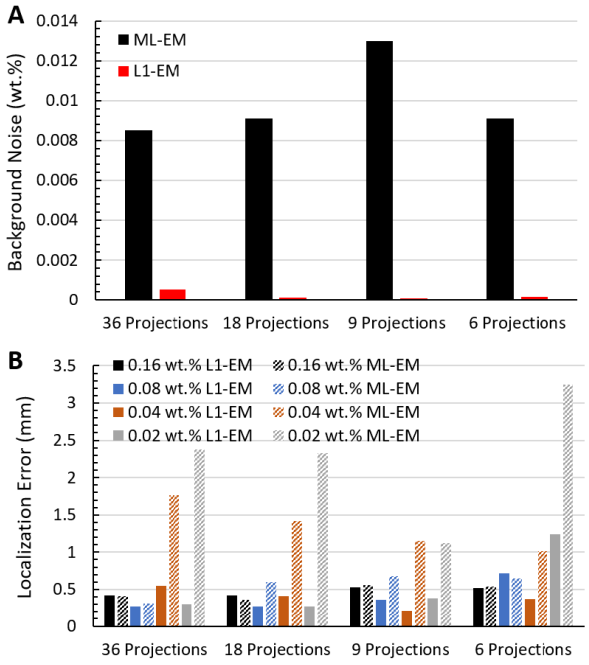

FIGURE 5. (A) Background noise of the XFCT images reconstructed from different number of projection views using ML-EM and L1-EM algorithms. (B) Localization errors of the four GNP targets reconstructed by ML-EM (diagonal stripe) and L1-EM (slid) algorithms, for the XFCT imaging with different number of projection views.

printer using polylactic acid printing material with polyvinyl alcohol, and filled with Agarose gel (2 wt.%) mixed with 0.15 wt.% GNP and 0.6 wt.% iodinated contrast agent Iopamidol (Fig. 6C). The GNP concentration was chosen to mimic the low concentration in tumor [23]. Iodinated contrast was employed to identify the small target via transmission CT (Figs. 6A and 6B), to evaluate the reconstruction accuracy of the sparse-view XFCT. Given the potentially large localization error in the 6-projection-view XFCT (as shown in Fig. 5B), projections from 9 views were collected in this experiment. Figures 6D-6E show the XFCT images reconstructed using ML-EM and L1-EM with different regularization parameters. Although ML-EM recovered the small GNP target, the adjacent artifact (marked by arrowhead in Fig. 6D) induces severe interference on the target detection. This interference was mitigated by L1-EM with sparsity regularization (Figs. 6E and 6F). However, too small regularization parameter (i.e. $\lambda = 0.05$ in Fig. 6E) just alleviated the artifact. In contrast, the artifact was eradicated by L1-EM with $\lambda = 0.1$ which matches the optimal regularization parameter adopted in the aforementioned phantom XFCT reconstruction with 9 projection views.

IV. DISCUSSION

As the number of projections decreases, the XFCT reconstruction inverse problem becomes increasingly ill-posed and sensitive to measured noise. In this investigation, we proposed an L1-EM algorithm for the spare-view XFCT reconstruction. The implementation of this algorithm takes into account the simplicity of the emission-EM-look-like algorithms and the robustness of L1-norm

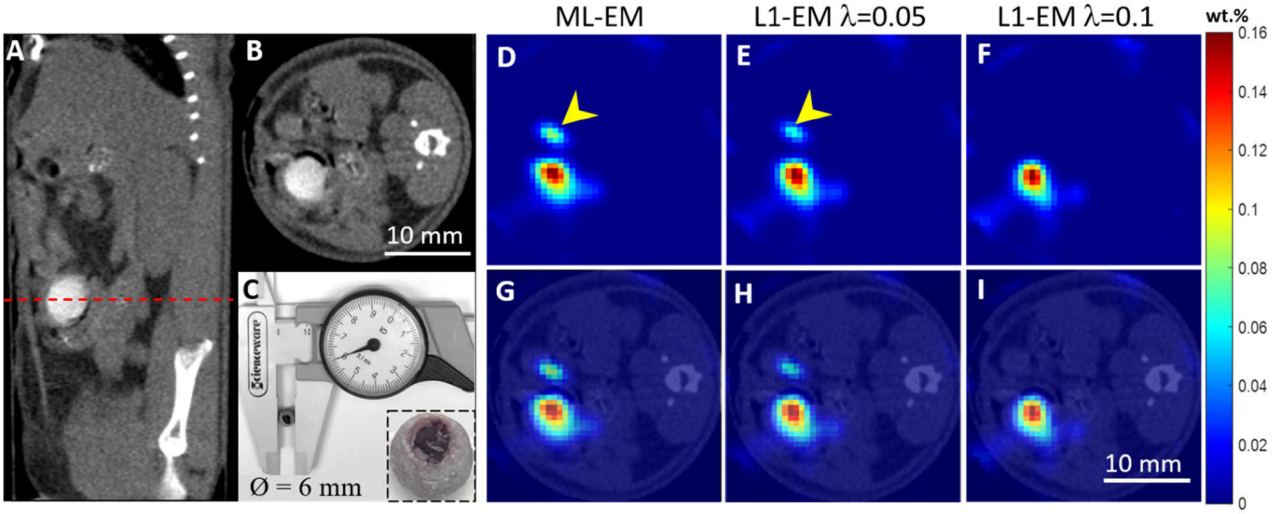

FIGURE 6. (A) A sagittal CT slice of a mouse surgically implanted with a small tumor-mimicking sphere. (B) An axial CT slice corresponding to the red dotted line in (A). (C) The 3D printed small hollow sphere (diameter: 6 mm) filled with gel mixed with GNPs and Iodine. Right corner insert shows the enlarged photograph of the implanted small sphere. (D-F) XFCT images reconstructed from 9 projection views by ML-EM and L1-EM with different regularization parameters. The arrowhead denotes the artifacts in the reconstruction. (G-I) Fused XFCT and CT images.

regularization against artifacts. The performance of the algorithms was evaluated via phantom and small animal experiments. The phantom results show that the proposed L1-EM algorithm can robustly suppress background artifacts and localize low-concentration GNPs (0.02 wt.%) with sub-millimeter accuracy, when the number of projection views reduces from 36 to 9. Under the current experimental setup, data collection costs 21 × 30 s per projection view, for a 3-cm-diameter phantom XFCT scanning. As the number of projection angles reduced from 36 to 9, the total scanning time per XFCT slice drops from 6.3 hrs to 1.6 hrs, and the corresponding imaging dose declines by 4 times. Moreover, if we implement the reduced-scan scheme [24], in which only the half of the object closest to the XRF detector is translationally scanned, the total XFCT scanning time and imaging dose will be reduced twice further.

As a kind of Green's one-step-late algorithm, the proposed L1-EM algorithm relies on an appropriate regularization parameter to achieve the expected results. The regularization parameter λ plays a critical role by trading off the reconstruction accuracy and the sparse regularization. Too small λ value induces weak noise suppression in the XFCT reconstruction. In this study, the optimal λ value was automatically selected by calculating the maximum of the L-curve. As the number of projection angles reduced from 36 to 18, 9, and 6, the λ values were correspondingly determined as 0.25, 0.15, 0.10, and 0.05. A smaller L1-EM λ value corresponds to the reconstruction with a lower number of projection views, which is explainable based on the tradeoff role the parameter λ plays. Moreover, sparsity in form of total variation (TV) can be incorporated into XFCT reconstruction. As demonstrated in our previously published study [32], combining with L1 regularization, TV could complementarily maintain the local smoothness and preserve the shape of targets. Nevertheless, it is challenging to select the optimal regularization parameters for both L1 and TV, in the scenarios of XFCT with different number of projection views. Although L-curve criterion has been widely used to determine the regularization parameter [33], a more robust hyperparameter selection strategy would substantially benefit sparse-view XFCT.

In the present study, a small-animal-size water phantom was employed to optimize the L1-EM regularization parameter. The size similarity leads to the similar system matrix and regularization parameter for the phantom and small animal XFCT reconstruction. One factor that limits XFCT reconstruction is the self-absorption effect which refers to the fact that the emitted x-ray fluorescence photons can be reabsorbed as they travel through the imaging object. The attenuation coefficients used in the current XFCT imaging model was assumed to be homogeneous, which is reasonable for the water phantom and mouse abdomen with sparse GNP targets. Nevertheless, constructing a more accurate mathematic model with heterogeneous attenuation characteristic is essential, especially for the sparse-view XFCT imaging of a large organ. In the scenario with the accurate attenuation correction [34], the phantom-calculated regularization parameter could be extended to small animal XFCT reconstruction with better robustness.

Sparse-view strategy with benefits of reducing imaging dose and reducing scan time has been widely studied and applied in transmission X-ray CT and X-ray luminescence CT [35]–[37]. In this study, we explored the potential of sparse-view strategy in pencil-beam XFCT imaging. As shown in the phantom experiments, when the number of projection views is too small (e.g. 6), there will exist deterioration of localization accuracy, especially for

the low-concentration (e.g. 0.02 wt.%) GNP target. Further *in vivo* small animal XFCT imaging is essential to study how the sparse views and the initial view position affect the reconstruction accuracy of actual GNP distribution. In the current experiments, the L-shell XRF photons emitted from GNPs were collected for XFCT imaging. The relatively high attenuation of the L-shell XRF photons is another source inducing the deteriorated localization accuracy of the low-concentration GNP targets. To alleviate the reconstruction error in sparse-view L-shell XFCT imaging, the benchtop pseudo-monoenergetic x-ray sources (e.g. polycapillary x-ray optic [22]) could be implemented to enhance the amount of the detectible XFR photons. Although the presented experiments were conducted on the L-shell XFCT system, it is expected that the proposed algorithm will be applied in sparse-view K-shell XFCT imaging.

V. CONCLUSION

This study presented an L1-EM reconstruction algorithm for sparse-view XFCT imaging to reduce the total scanning time and imaging dose. The performance of the proposed algorithm was validated through phantom and small animal XFCT imaging with sparse-view projections. The proposed algorithm can robustly suppress artifacts and achieve submillimeter-level localization accuracy for the targets with GNP concentration as low as 0.02 wt.%, even for the XFCT imaging with only 9 projection views. Combination of the proposed reconstruction algorithm with further system upgrade could enable further fast *in vivo* XFCT imaging.

REFERENCES

[1] N. Manohar, F. J. Reynoso, P. Diagaradjane, S. Krishnan, and S. H. Cho, "Quantitative imaging of gold nanoparticle distribution in a tumor-bearing mouse using benchtop X-ray fluorescence computed tomography," *Sci. Rep.*, vol. 6, no. 1, p. 22079, Apr. 2016.

[2] S. Zhang, L. Li, J. Chen, Z. Chen, W. Zhang, and H. Lu, "Quantitative imaging of gd nanoparticles in mice using benchtop cone-beam X-ray fluorescence computed tomography system," *Int. J. Mol. Sci.*, vol. 20, no. 9, p. 2315, May 2019.

[3] D. Peer, J. M. Karp, S. Hong, O. C. Farokhzad, R. Margalit, and R. Langer, "Nanocarriers as an emerging platform for cancer therapy," *Nature Nanotechnol.*, vol. 2, no. 12, p. 751, 2007.

[4] P. Boisseau and L. Grodzins, "Fluorescence tomography using synchrotron radiation at the NSLS," *Hyperfine Interact.*, vol. 33, nos. 1–4, pp. 283–292, 1987.

[5] R. Cesareo and S. Mascarenhas, "A new tomographic device based on the detection of fluorescent X-rays," *Nucl. Instrum. Methods Phys. Res. A, Accel. Spectrom. Detect. Assoc. Equip.*, vol. 277, nos. 2–3, pp. 669–672, May 1989.

[6] T. Takeda, "Preliminary experiment of the fluorescent X-ray computed tomography with synchorotron radiation," *Med. Imag. Technol.*, vol. 12, pp. 537–538, Nov. 1994.

[7] T. Takeda, T. Yuasa, A. Hoshino, M. Akiba, A. Uchida, M. Kazama, K. Hyodo, F. A. Dilmanian, T. Akatsuka, and Y. Itai, "Fluorescent X-ray computed tomography to visualize specific material distribution," *Proc. SPIE*, vol. 3149, pp. 160–172, Oct. 1997.

[8] S.-K. Cheong, B. L. Jones, A. K Siddiqi, F. Liu, N. Manohar, and S. H. Cho, "X-ray fluorescence computed tomography (XFCT) imaging of gold nanoparticle-loaded objects using 110 kVp X-rays," *Phys. Med. Biol.*, vol. 55, no. 3, pp. 647–662, Feb. 2010.

[9] N. Manohar, F. J. Reynoso, and S. H. Cho, "Experimental demonstration of direct l -shell X-ray fluorescence imaging of gold nanoparticles using a benchtop X-ray source," *Med. Phys.*, vol. 40, no. 8, Jul. 2013, Art. no. 080702.

[10] L. Ren, D. Wu, Y. Li, G. Wang, X. Wu, and H. Liu, "Three-dimensional X-ray fluorescence mapping of a gold nanoparticle-loaded phantom," *Med. Phys.*, vol. 41, no. 3, Feb. 2014, Art. no. 031902.

[11] A. Groll, J. George, P. Vargas, P. J. La Riviere, and L. J. Meng, "Element mapping in organic samples utilizing a benchtop X-ray fluorescence emission tomography (XFET) system," *IEEE Trans. Nucl. Sci.*, vol. 62, no. 5, pp. 2310–2317, Oct. 2015.

[12] K. Ricketts, C. Guazzoni, A. Castoldi, and G. Royle, "A bench-top k X-ray fluorescence system for quantitative measurement of gold nanoparticles for biological sample diagnostics," *Nucl. Instrum. Methods Phys. Res. A, Accel. Spectrom. Detect. Assoc. Equip.*, vol. 816, pp. 25–32, Apr. 2016.

[13] M. Bazalova-Carter, M. Ahmad, L. Xing, and R. Fahrig, "Experimental validation of L-shell X-ray fluorescence computed tomography imaging: Phantom study," *J. Med. Imag.*, vol. 2, no. 4, Oct. 2015, Art. no. 043501.

[14] Y. Kuang, G. Pratx, M. Bazalova, B. Meng, J. Qian, and L. Xing, "First demonstration of multiplexed X-ray fluorescence computed tomography (XFCT) imaging," *IEEE Trans. Med. Imag.*, vol. 32, no. 2, pp. 262–267, Feb. 2013.

[15] B. L. Jones and S. H. Cho, "The feasibility of polychromatic cone-beam X-ray fluorescence computed tomography (XFCT) imaging of gold nanoparticle-loaded objects: A Monte Carlo study," *Phys. Med. Biol.*, vol. 56, no. 12, p. 3719, 2011.

[16] S. Jiang, P. He, L. Deng, M. Chen, and B. Wei, "Monte Carlo simulation for polychromatic X-ray fluorescence computed tomography with sheet-beam geometry," *Int. J. Biomed. Imag.*, vol. 2017, pp. 1–10, May 2017.

[17] C. A. S. Dunning and M. Bazalova-Carter, "Optimization of a table-top X-ray fluorescence computed tomography (XFCT) system," *Phys. Med. Biol.*, vol. 63, no. 23, Nov. 2018, Art. no. 235013.

[18] L. Li, S. Zhang, R. Li, and Z. Chen, "Full-field fan-beam X-ray fluorescence computed tomography with a conventional X-ray tube and photon-counting detectors for fast nanoparticle bioimaging," *Opt. Eng.*, vol. 56, no. 4, Apr. 2017, Art. no. 043106.

[19] S. Jung, T. Kim, W. Lee, H. Kim, H. S. Kim, H. J. Im, and S. J. Ye, "Dynamic *in vivo* X-ray fluorescence imaging of gold in living mice exposed to gold nanoparticles," *IEEE Trans. Med. Imag.*, vol. 39, no. 2, pp. 526–533, Feb. 2020.

[20] T. Sasaya, N. Sunaguchi, K. Hyodo, T. Zeniya, and T. Yuasa, "Multi-pinhole fluorescent X-ray computed tomography for molecular imaging," *Sci. Rep.*, vol. 7, no. 1, pp. 1–12, 2017.

[21] D. Vernekohl, M. Ahmad, G. Chinn, and L. Xing, "Feasibility study of Compton cameras for X-ray fluorescence computed tomography with humans," *Phys. Med. Biol.*, vol. 61, no. 24, p. 8521, 2016.

[22] D. Vernekohl, M. Ahmad, X. Dai, W. Zhao, K. Cheng, and L. Xing, "Reduced acquisition time for L-shell X-ray fluorescence computed tomography using polycapillary X-ray optics," *Med. Phys.*, vol. 46, no. 12, pp. 5696–5702, Dec. 2019.

[23] J. C. Larsson, C. Vogt, W. Vågberg, M. S. Toprak, J. Dzieran, M. Arsenian-Henriksson, and H. M. Hertz, "High-spatial-resolution X-ray fluorescence tomography with spectrally matched nanoparticles," *Phys. Med. Biol.*, vol. 63, no. 16, Aug. 2018, Art. no. 164001.

[24] P. J. La Riviere, P. Vargas, M. Newville, and S. R. Sutton, "Reduced-scan schemes for X-ray fluorescence computed tomography," *IEEE Trans. Nucl. Sci.*, vol. 54, no. 5, pp. 1535–1542, Oct. 2007.

[25] H. Kudo, T. Suzuki, and E. Rashed, "Image reconstruction for sparse-view CT and interior CT-introduction to compressed sensing and differentiated backprojection," *Quant. Imag. Med. Surg.*, vol. 3, no. 3, p. 147, 2013.

[26] R. Bazak, M. Houri, S. El Achy, S. Kamel, and T. Refaat, "Cancer active targeting by nanoparticles: A comprehensive review of literature," *J. Cancer Res. Clin. Oncol.*, vol. 141, no. 5, pp. 769–784, May 2015.

[27] L. A. Feldkamp, L. C. Davis, and J. W. Kress, "Practical cone-beam algorithm," *J. Opt. Soc. Amer. A, Opt. Image Sci. 1, no.*, vol. 6, no. 1984, pp. 612–619.

[28] M. Ahmad, M. Bazalova-Carter, R. Fahrig, and L. Xing, "Optimized detector angular configuration increases the sensitivity of X-ray fluorescence computed tomography (XFCT)," *IEEE Trans. Med. Imag.*, vol. 34, no. 5, pp. 1140–1147, May 2015.

[29] G. L. Zeng, *Medical Image Reconstruction: A Conceptual Tutorial*. New York, NY, USA: Springer, 2010.

[30] P. C. Hansen and D. P. O'Leary, "The use of the L-Curve in the regularization of discrete ill-posed problems," *SIAM J. Sci. Comput.*, vol. 14, no. 6, pp. 1487–1503, Nov. 1993.

[31] L. Deng, M. F. Ahmed, S. Jayarathna, P. Feng, B. Wei, and S. H. Cho, "A detector's eye view (DEV)-based OSEM algorithm for benchtop X-ray fluorescence computed tomography (XFCT) image reconstruction," *Phys. Med. Biol.*, vol. 64, no. 8, Apr. 2019, Art. no. 08NT02.
[32] J. Shi, B. Granger, K. Xu, and Y. Yang, "Quantitative X-ray fluorescence imaging of gold nanoparticles using joint L1 and total variation regularized reconstruction," *Quant. Imag. Med. Surg.*, vol. 10, no. 1, p. 184, 2020.
[33] X. Yang, R. Hofmann, R. Dapp, T. van de Kamp, T. dos Santos Rolo, X. Xiao, J. Moosmann, J. Kashef, and R. Stotzka, "TV-based conjugate gradient method and discrete L-curve for few-view CT reconstruction of X-ray *in vivo* data," *Opt. Express*, vol. 23, no. 5, pp. 5368–5387, 2015.
[34] Q. Yang, B. Deng, G. Du, H. Xie, G. Zhou, T. Xiao, and H. Xu, "X-ray fluorescence computed tomography with absorption correction for biomedical samples," *X-Ray Spectrometry*, vol. 43, no. 5, pp. 278–285, Sep. 2014.
[35] Z. Hu, J. Gao, N. Zhang, Y. Yang, X. Liu, H. Zheng, and D. Liang, "An improved statistical iterative algorithm for sparse-view and limited-angle CT image reconstruction," *Sci. Rep.*, vol. 7, no. 1, pp. 1–9, Dec. 2017.
[36] P. Gao, J. Rong, T. Liu, W. Zhang, B. Lan, X. Ouyang, and H. Lu, "Limited view cone-beam X-ray luminescence tomography based on depth compensation and group sparsity prior," *J. Biomed. Opt.*, vol. 25, no. 1, Jan. 2020, Art. no. 016004.
[37] P. Gao, J. Rong, H. Pu, T. Liu, W. Zhang, X. Zhang, and H. Lu, "Sparse view cone beam X-ray luminescence tomography based on truncated singular value decomposition," *Opt. Express*, vol. 26, no. 18, pp. 23233–23250, 2018.

JUNWEI SHI received the Ph.D. degree in biomedical engineering from Tsinghua University, China, in 2015. He is currently a Research Assistant Professor with the Radiation Oncology Department, University of Miami. His research interests include X-ray computed tomography, bioluminescence tomography, fluorescence molecular tomography, X-ray fluorescence computed tomography, MRI, reconstruction algorithm, and the application of multi-modality imaging in preclinical radiotherapy research.

DAIKI HARA is currently pursuing the Ph.D. degree in medical physics with the Biomedical Engineering Department, University of Miami. His research interests include X-ray fluorescence computed tomography, MRI, and the development and application of active targeting nanoparticle in image-guided radiosensitization.

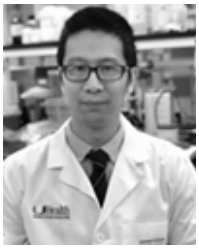

WENSI TAO received the Ph.D. degree in molecular cell and developmental biology from the University of Miami, in 2015. He is currently a Research Assistant Professor with the Radiation Oncology Department, University of Miami. His research interests include developing clinically relevant prostate cancer models, such as patient derived xenograft, genetically modified animal models and 3D cancer spheroids for radiotherapy, and prostate specific targeted therapy.

NESRIN DOGAN received the Ph.D. degree in nuclear engineering from the University of Michigan, Ann Arbor, MI, USA. She is currently a Professor with the Radiation Oncology Department, University of Miami. Her research interests include medical imaging, image processing, and image guided adaptive radiation therapy.

ALAN POLLACK received the Ph.D. degree in microbiology and immunology from the University of Miami and the M.D. degree from the Miller School of Medicine, University of Miami. He is currently a Professor with the Radiation Oncology Department, University of Miami. His research interest includes the therapeutic management of prostate cancer, with an emphasis on applying biomarkers, including quantitative imaging, tissue genomic, and liquid biopsy markers, to identify prostate characteristics that determine outcome.

JOHN CHETLEY FORD received the Ph.D. degree in physics from the University of Connecticut, Mansfield, CT, USA. He is currently an Associate Professor with the Radiation Oncology Department, University of Miami. His research interests include MRI system development, MRI image processing, MRI-guided radiation therapy, and the application of MRI in targeting and assessing response to radiation therapy.